Jonathan Realmuto
Department of Mechanical Engineering,
University of Washington,
Seattle, WA 98195
e-mail: realmuto@uw.edu

Glenn Klute
Department of Veterans Affairs,
Center of Excellence for Limb Loss,
Prevention and Prosthetic Engineering,
Seattle, WA 98195;
Department of Mechanical Engineering,
University of Washington,
Seattle, WA 98195
e-mail: gklute@uw.edu

Santosh Devasia
Department of Mechanical Engineering,
University of Washington,
Seattle, WA 98195
e-mail: devasia@uw.edu

Nonlinear Passive Cam-Based Springs for Powered Ankle Prostheses

This article studies the design of passive elastic elements to reduce the actuator requirements for powered ankle prostheses. The challenge is to achieve most of the typically nonlinear ankle response with the passive element so that the active ankle-torque from the actuator can be small. The main contribution of this article is the design of a cam-based lower-limb prosthesis to achieve such a nonlinear ankle response. Results are presented to show that the addition of the cam-based passive element can reduce the peak actuator torque requirement substantially, by ~74%. Moreover, experimental results are presented to demonstrate that the cam-based design can achieve a desired nonlinear response to within 10%. [DOI: 10.1115/1.4028653]

1 Introduction

This article studies the design of passive parallel elements to reduce the actuator requirements (e.g., energy, power, and torque) for powered ankle prostheses. Improvements in powered lower-limb prostheses have the potential to benefit 1.4% of the general population in the US who require the use of an artificial leg or foot [1]. Moreover, amputations in the geriatric population in the US are expected to double from 28,000 to 58,000 per year by 2030 [2]. In particular, passive elements parallel to the actuator can reduce the maximum ankle-torque requirement and, thereby, reduce the actuator size in powered lower-limb prostheses, e.g., Ref. [3]. By reducing the size of the actuator, used to supply the active ankle torque required for fuller restoration of lower-limb function [4–8], the size and weight of the powered prostheses can be kept similar to that of the missing limb. In turn, the actuator size can be reduced by decreasing the maximum required actuator torque, e.g., as shown for electric motors in Ref. [9]. The challenge, however, is to achieve most of the typically nonlinear ankle response with the passive element so that the required active ankle-torque from the actuator can be small. The main contribution of this article is the design of a cam-based device to optimally match the desired nonlinear response of the parallel elastic element in ankle prostheses.

There is substantial research on the design of passive elastic devices to achieve a specified nonlinear response, e.g., see review article [10]. One approach is to tailor the geometry (splined cantilevers or conical springs) and material properties such that the elastic properties vary as the spring displaces, e.g., Ref. [11]. In lower-limb prostheses, on–off type nonlinearities have been introduced through unidirectional elastic elements [12], and clutch or locking mechanisms [13–16]. Mechanisms such as four-bar linkages [3] and hypocycloids [17] can be used to exactly match several points on the elastic (force–displacement) response by selecting a finite number of design parameters such as the link-lengths of the four-bar mechanism or radii of the circles generating the hypocycloids. In addition, these parameters can be used to achieve the best fit possible of the desired elastic response. In comparison to other mechanisms, cam-based designs have more design flexibility (i.e., in the choice of the cam profile) and can, therefore, be used to match a substantially larger segment of the force–displacement curve, e.g., as in Refs. [18–20]. Such a cam-based design is adapted in this article for lower-limb prostheses, which is a generalization of previous work [21] that used a cam-based device for shock absorption.

The ability to walk comfortably in an urban environment received the highest rankings among lower-limb amputees in a study examining prosthesis-related issues of importance [22]. Therefore, the current article aims to match the nonlinear passive response of an ankle for a specific self-selected walking gait. Variations in the ankle response, due to different walking conditions, would then be accommodated by the actuator. If a wide range of gaits are expected, then the current approach could be extended by optimizing the cam profile to best fit the ankle response over a range of walking conditions [23]. Alternatively, variable stiffness elements, which use motors to change the spring preload or adjust the transmission ratio between actuator and spring, e.g., Ref. [10], can be used to adapt for different gaits. Nevertheless, since the majority of prosthesis usage is for self-selected walking, this article focusses on optimizing the passive cam-design for a single gait as in previous works, e.g., Ref. [3]. For the selected gait (data from Ref. [24]) the cam-based nonlinear design can: (i) reduce the overall actuator torque requirement substantially, by ~74%; (ii) yield better performance than a linear design, e.g., reduce peak actuator torque by ~21% when compared with a linear design. Passive bench test results are presented to experimentally demonstrate that the current cam-based prototype can achieve the desired nonlinear response to within 10%.

2 The Design Problem

This section begins with a brief background on human gait and a description of the gait trajectory used in this study to design the cam-based spring.

2.1 Human Gait Background. The gait cycle begins with heel strike (HS) of one leg and ends with the next HS of same leg. Foot flat (FF) occurs after HS when the whole foot makes contact with the ground. FF marks a transition from plantarflexion to

Manuscript received July 16, 2014; final manuscript received September 15, 2014; published online November 14, 2014. Assoc. Editor: Rita M. Patterson.

This material is declared a work of the U.S. Government and is not subject to copyright protection in the United States. Approved for public release; distribution is unlimited.

Downloaded From: http://medicaldevices.asmedigitalcollection.asme.org/ on 12/15/2014 Terms of Use: http://asme.org/terms

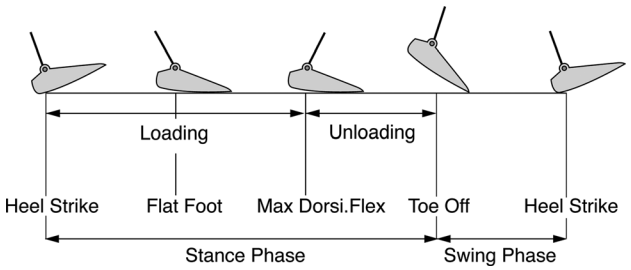

Fig. 1 Biomechanics of level ground walking. The gait cycle can be divided into a stance phase and a swing phase.

Table 1 Subject gait parameters for reference trajectory [24]

Mass M (kg)	Height (m)	Mean leg length (m)	Age (yr)	Gait speed (m/s)
84.4	1.82	0.97	27	1.21

dorsiflexion, where dorsiflexion is defined as the ankle motion that brings the toes closer to the shin, and plantarflexion is defined as ankle motion in the opposite direction. The following sign conventions are used throughout the article: ankle displacement is considered positive for dorsiflexion, and a torque promoting dorsiflexion is considered to be positive. Zero ankle position is assigned to the position where the foot segment is perpendicular to the shank (or shin) segment. The next gait event is maximum dorsiflexion (MDF), which marks a transition from dorsiflexion to plantarflexion. The last event, toe-off (TO), is defined as the instant when the toe leaves the ground. The stance phase, about 60% of the gait cycle, begins with HS and ends with TO. The remaining 40% of the gait cycle is called swing phase, and is characterized by the foot being off the ground. In this article, the stance phase is separated into a period of loading followed by a period of unloading. Loading occurs from HS to MDF, and unloading occurs from MDF to TO. Figure 1 summarizes the events and phases of level ground gait.

2.2 Desired Gait Trajectory. The desired (reference) gait trajectory used in this study is for level ground walking at self-selected speed (the data is from Ref. [24]). Table 1 gives the details of the subject. The associated desired angular displacement θ_d, torque T_d, and power P_d time-trajectories are shown in Fig. 2. The corresponding ankle stiffness characteristics of the stance phase, or equivalently the torque–displacement relationship, is shown in Fig. 3. This trajectory has a small hysteresis loop, and is consistent with the typical gait at self-selected walking speed [7]. In the following, the powered ankle prosthesis will follow these desired angular displacement θ_d and torque T_d trajectories.

2.3 Design Issues. The design problem is to effectively mimic the ankle stiffness characteristics shown in Fig. 3 over different parts of the stance phase. Moreover, negative power represents ankle power absorption, and positive power corresponds to ankle power generation [25]. Therefore, an ideal device should maximize absorption of energy by passive components during the loading phase of stance (from HS to MDF) and release energy during the unloading phase of stance.

3 Modeling and Optimization

Two configurations for the elastic elements in powered ankle prostheses are: parallel elastic actuator (PEA) [12,23,26–28] and series elastic actuator (SEA) [12,29,30], as illustrated in Fig. 4. A series elastic element (spring k_s) can increase shock tolerance and decrease reflected inertia [31], but cannot reduce torque

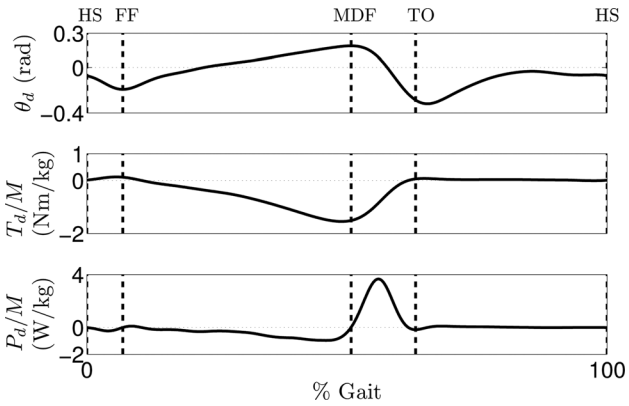

Fig. 2 Gait trajectories for nonamputee walking at self-selected walking speed [24]. The dotted lines represent the phase transitions from Fig. 1. Top: angular displacement θ_d during the gait cycle. Middle: ankle-torque T_d normalized by body mass *M*. Bottom: ankle power P_d normalized by body mass *M*.

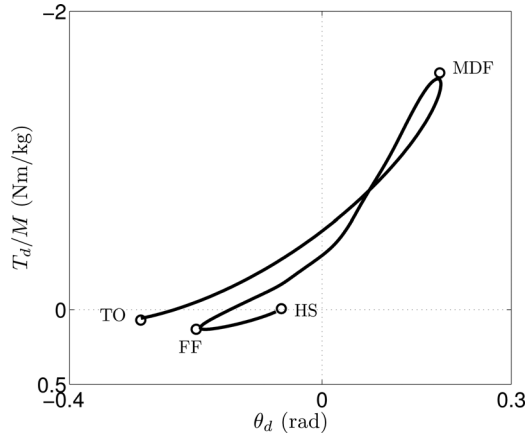

Fig. 3 Ankle-joint stiffness characteristics (ankle-torque T_d normalized by body mass *M* versus angular displacement θ_d) during stance phase for self-selected walking speed. The loading phase begins with HS and ends with MDF. Unloading begins with MDF and ends with TO.

requirement because the actuator torque T_a must supply the reference torque T_d, i.e.,

$$T_a = -k_s(\theta_d - \theta_a) = T_d \tag{1}$$

where θ_d is the desired angular displacement and θ_a is the actuator displacement. Reducing the actuator torque needs a parallel elastic element [12,23,26–28]. Hence, this analysis focusses on the optimization of the parallel elastic element.

3.1 PEA Model. The PEA configuration is illustrated in Fig. 4. In order to achieve the desired reference torque T_d (shown in Fig. 2), the actuator must provide the residual active torque T_a, i.e., the difference between the desired torque T_d and the torque T_p produced by the parallel spring

$$T_a = T_d - T_p \tag{2}$$

For a linear passive spring the torque T_p can be expressed in terms the of angular displacement θ_d and spring constant k_p as

$$T_p = -k_p\theta_d - k_0 \tag{3}$$

Downloaded From: http://medicaldevices.asmedigitalcollection.asme.org/ on 12/15/2014 Terms of Use: http://asme.org/terms

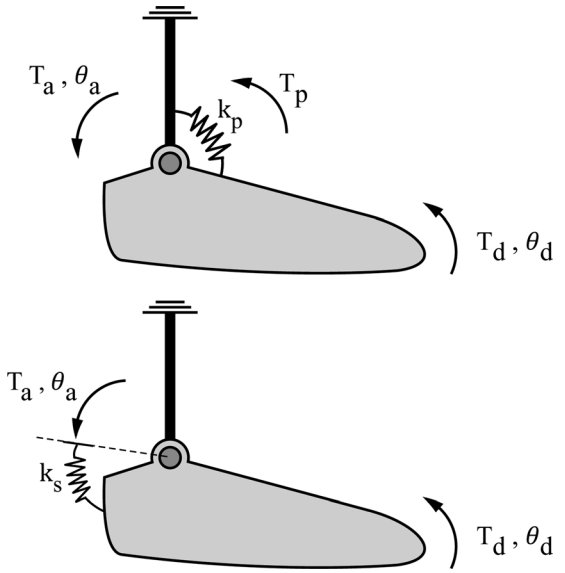

Fig. 4 Schematic representations of 1DOF powered ankle configurations. (Top) The PEA configuration is characterized by an ideal torque source T_a in parallel with a rotational passive component. The parallel component generates a torque T_p as a function of the angular displacement θ_d. (Bottom) The SEA configuration consists of an ideal torque source T_a in series with a rotational passive component.

where k_0 is the preload of the spring. This expression can be generalized for a nonlinear nth degree polynomial spring to

$$T_p = -\sum_{i=0}^{n} \theta_d^i k_{p_i} = -\Theta_n^T \mathbf{k}_p \tag{4}$$

where transpose is denoted by superscript T, Θ_n is a vector containing a geometric progression of θ_d up to power n

$$\Theta_n = \begin{bmatrix} 1 & \theta_d^1 & \theta_d^2 \cdots \theta_d^n \end{bmatrix}^T \tag{5}$$

and the vector $\mathbf{k}_p$ contains the $n+1$ nonlinear spring parameters

$$\mathbf{k}_p = \begin{bmatrix} k_{p,0} & k_{p,1} \cdots k_{p,n} \end{bmatrix}^T \tag{6}$$

The active power P_a (the active torque T_a multiplied by the angular velocity of the actuator $\dot{\theta}_a$) can be expressed as

$$P_a = T_a \dot{\theta}_a = T_d \dot{\theta}_d + \left(\Theta_n^T \mathbf{k}_p\right)\dot{\theta}_d \tag{7}$$

where the actuator displacement θ_a is identically the desired angular displacement θ_d.

3.2 Optimization. The goal of the optimization is to choose PEA spring parameter $\mathbf{k}_p$ such that the smallest actuator and energy resources can be used to maintain the reference trajectory. Therefore, the optimization seeks to minimize the peak torque $T_{a,p}$ and positive peak power $P_{a,p}^+$ over the entire gait cycle. It is noted that the negative mechanical power is not penalized in the optimization, as it can potentially be stored and reused as well, e.g., by converting to electrical energy [12]. Additionally, a penalty on the positive mechanical energy, E_a^+, used during a gait cycle, is added to yield the following minimization problem:

$$\min_{\mathbf{k}_p} \quad w_1 E_a^+ + w_2 P_{a,p}^+ + w_3 T_{a,p} \tag{8}$$

where $\mathbf{k}_p$ are the spring parameters to be optimized and the weighting parameters can be expressed as a vector $\mathbf{w}$

$$\mathbf{w} = \begin{bmatrix} w_1 & w_2 & w_3 \end{bmatrix} \tag{9}$$

In the above minimization problem (in Eq. (8)), the peak torque supplied by the active component $T_{a,p}$ is defined as the maximum absolute value of the active torque over all sampled values in the entire gait cycle, i.e.,

$$T_{a,p} := \max_{i \in \{1,\cdots,p\}} \left| T_d[i] + \Theta_n^T[i]\mathbf{k}_p \right| \tag{10}$$

where $[i]$ represents the ith sample, and p is the total number of samples. The power P_a can be decomposed into positive P_a^+ and negative P_a^- parts, where

$$\begin{aligned} P_a^+ &= \frac{1}{2}\left(P_a + |P_a|\right) \\ &= \frac{1}{2}\left(T_d\dot{\theta}_d + \left(\Theta_n^T\mathbf{k}_p\right)\dot{\theta}_d + \left|T_d\dot{\theta}_d + \left(\Theta_n^T\mathbf{k}_p\right)\dot{\theta}_d\right|\right) \end{aligned} \tag{11}$$

and

$$\begin{aligned} P_a^- &= \frac{1}{2}\left(P_a - |P_a|\right) \\ &= \frac{1}{2}\left(T_d\dot{\theta}_d + \left(\Theta_n^T\mathbf{k}_p\right)\dot{\theta}_d - \left|T_d\dot{\theta}_d + \left(\Theta_n^T\mathbf{k}_p\right)\dot{\theta}_d\right|\right) \end{aligned} \tag{12}$$

Then the positive peak power is defined as the maximum over all sampled values in the entire gait cycle, i.e.,

$$P_{a,p}^+ := \max_{i \in \{1,\cdots,p\}} P_a^+[i] \tag{13}$$

Positive and negative mechanical energy requirements are defined as the integral of positive and negative power, respectively, and are given by

$$E_a^+ = \int_0^T P_a(t)^+ dt \approx \sum_{i=1}^{p} P_a[i]^+ \Delta_t \tag{14}$$

$$E_a^- = \int_0^T P_a(t)^- dt \approx \sum_{i=1}^{p} P_a[i]^- \Delta_t \tag{15}$$

where $\Delta_t = T/p$ is the sampling period and the integral is approximated with the sampled values.

The minimization problem in Eq. (8) is a convex optimization problem, since the objective function is a summation of convex functions with optimization variable $\mathbf{k}_p$ appearing linearly in the expressions for peak torque (Eq. (10)), peak positive power (Eq. (13)), and positive energy (Eq. (14)). Hence, standard optimization algorithms can be used to solve the optimization problem in Eq. (8), and global optimality can be guaranteed [32].

3.3 Optimization Results. In this section, performance of the different configurations is quantified. First, a comparison between a linear and nonlinear PEA reveals that a nonlinear PEA can significantly decrease the torque requirement of the active component. Additionally, the decrease in torque requirement can be traded off to reduce the positive energy requirement and the positive peak power by appropriately choosing the weights in Eq. (9).

3.3.1 Torque Reduction With Nonlinear PEA. Toward reducing the actuator torque, optimal spring parameters were found for PEA_n (i.e., different n in Eq. (4)) using the objective function Eq. (8) with weighting on only the peak torque (i.e., $\mathbf{w} = [0\ 0\ 1]$), where the polynomial order n of the PEA is denoted with a subscript. The effect of polynomial degree on each component of the

Downloaded From: http://medicaldevices.asmedigitalcollection.asme.org/ on 12/15/2014 Terms of Use: http://asme.org/terms

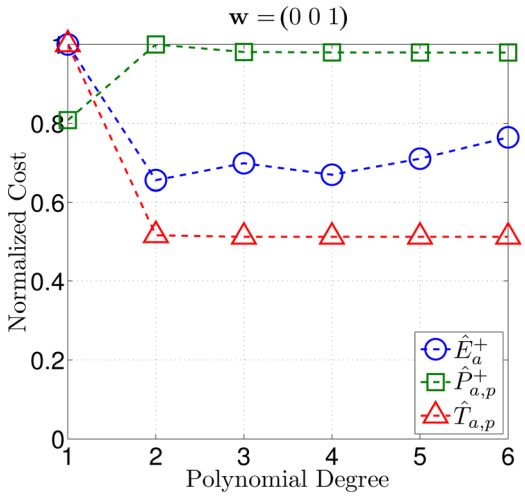

Fig. 5 Normalized component costs (Eq. (16)) versus polynomial degree *n* for optimal PEA. The optimization weights are w = [0 0 1] in Eq. (9).

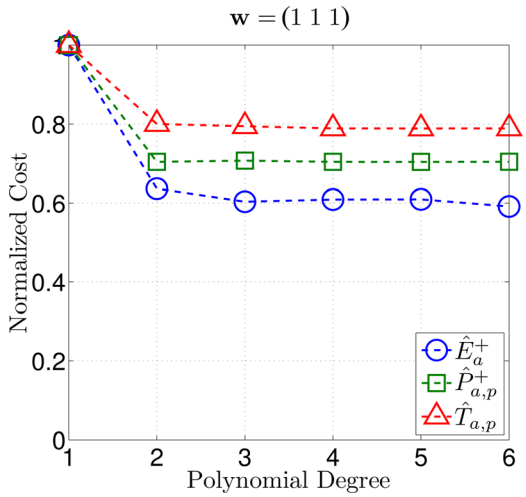

Fig. 6 Normalized component costs (Eq. (16)) versus polynomial degree *n* for optimal PEA. The optimization weights are w = [1 1 1] in Eq. (9).

objective function, Eq. (8), is shown in Fig. 5, where each component has been normalized to the common scale [0, 1], e.g.,

$$\hat{E}_{\mathrm{a}}^{+}(n) = \frac{E_{\mathrm{a}}^{+}(n)}{\max\limits_{j\in\{1,\ldots,6\}} E_{\mathrm{a}}^{+}(j)}$$
$$\hat{P}_{\mathrm{a,p}}^{+}(n) = \frac{P_{\mathrm{a,p}}^{+}(n)}{\max\limits_{j\in\{1,\ldots,6\}} P_{\mathrm{a,p}}^{+}(j)} \qquad (16)$$
$$\hat{T}_{\mathrm{a,p}}(n) = \frac{T_{\mathrm{a,p}}(n)}{\max\limits_{j\in\{1,\ldots,6\}} T_{\mathrm{a,p}}(j)}$$

and (n) corresponds to the polynomial degree. There is a large decrease (48.4%) in the peak torque between the linear PEA_1 and second-order nonlinear PEA_2 element. However, performance plateaus as the order n of the nonlinearity is increased; only marginal performance increases are realized with higher orders and the peak torque decrease is 48.8% between the linear PEA_1 and sixth order nonlinear PEA_6.

3.3.2 Mixed Weighting. Optimizing the nonlinear spring to reduce only the peak torque requirement results in a large torque reduction. However, a consequence is an increase in the power requirement, e.g., the positive peak power $P_{\mathrm{a,p}}^{+}$ increased by 23.7% between the linear PEA_1 and nonlinear PEA_2 as seen in Fig. 5. The optimization weights $\mathbf{w}$ in Eq. (9) can be chosen to trade-off the reduction in peak torque $T_{\mathrm{a,p}}$ to decrease the peak positive power $P_{\mathrm{a,p}}^{+}$. To illustrate, optimizations were performed for different degree n nonlinear PEA_n with the weighting chosen as $\mathbf{w} = [1\ 1\ 1]$, which penalizes all three: positive energy, peak positive power, and peak torque. The effect of polynomial degree on each component of the objective function, Eq. (8), is shown in Fig. 6. A reduction in all components of the objective function is realized with increasing polynomial order, but the benefits plateau after polynomial degree $n = 3$, and hence a third-degree nonlinear PEA_3 provides sufficient nonlinearity, and is selected as the nonlinearity to be achieved with a cam device in the following.

To illustrate the advantage of a nonlinear design over a linear design, Fig. 7 and Table 2 compare the performance of the linear PEA_1 and the nonlinear PEA_3 optimized with two different weights: $\mathbf{w} = [0\ 0\ 1]$ (optimized for torque only) and $\mathbf{w} = [1\ 1\ 1]$ (optimized for energy, power, and torque). Note, the PEA_3 with unity weights ($\mathbf{w} = [1\ 1\ 1]$) can reduce the positive energy and positive peak power without substantially giving up the reduction in peak torque as seen in Table 2. Moreover, the passive stiffness characteristics (e.g., torque–displacement relationship) of the third-degree nonlinear PEA_3 with $\mathbf{w} = [1\ 1\ 1]$ is closer to the desired ankle properties when compared to the linear PEA_1 as seen in Fig. 8. Thus, the closer match results in a reduction of actuator requirements as seen in Fig. 9. In particular, the actuator

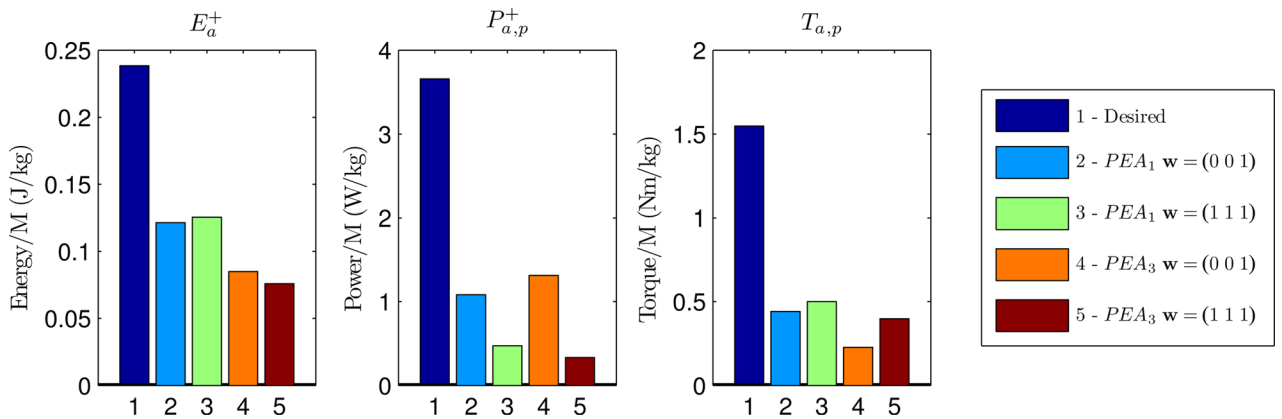

Fig. 7 Performance comparison of PEAs: positive energy E_{a}^{+} (left); peak positive peak power $P_{\mathrm{a,p}}^{+}$ (middle); and peak torque $T_{\mathrm{a,p}}$ (right)

Downloaded From: http://medicaldevices.asmedigitalcollection.asme.org/ on 12/15/2014 Terms of Use: http://asme.org/terms

Table 2 Comparison of PEA performance in Fig. 7

	E_a^+/M (J/kg)	$P_{a,p}^+/M$ (W/kg)	$T_{a,p}/M$ (N m/kg)
Desired	0.2384	3.6601	1.5475
PEA_1 $\mathbf{w}=[0\ 0\ 1]$	0.1215	1.0806	0.4404
PEA_1 $\mathbf{w}=[1\ 1\ 1]$	0.1256	0.4719	0.4996
PEA_3 $\mathbf{w}=[0\ 0\ 1]$	0.0849	1.3111	0.2257
PEA_3 $\mathbf{w}=[1\ 1\ 1]$	0.0758	0.3337	0.3970

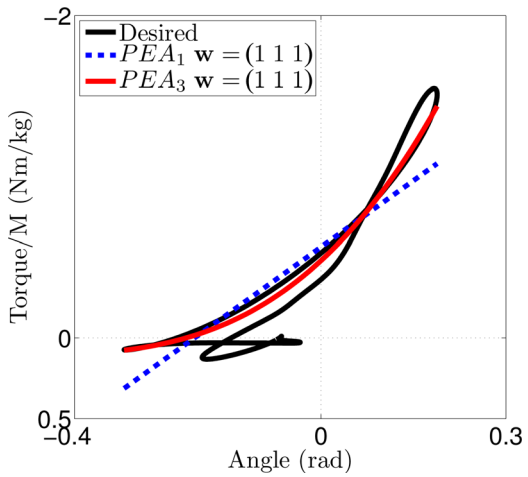

Fig. 8 The nonamputee ankle stiffness characteristics (normalized torque *T/M* versus desired angular displacement θ_d) for the entire gait cycle, superimposed with the linear PEA_1 and third-degree nonlinear PEA_3 stiffness profiles

requirements for the third-degree nonlinear PEA_3 with $\mathbf{w}=[1\ 1\ 1]$ are smaller than the linear PEA_1 with $\mathbf{w}=[1\ 1\ 1]$, i.e., are decreased by ~40%, ~29%, and ~21%, for positive energy, peak positive power, and peak torque, respectively, as seen by comparing the third and fifth row in Table 2. Moreover, the actuator requirements for the third-degree nonlinear PEA_3 with $\mathbf{w}=[1\ 1\ 1]$ are substantially smaller than the case without the PEA, i.e., are decreased by ~68%, ~91%, and ~74%, for positive energy, peak positive power, and peak torque, respectively, as seen by comparing the first and fifth rows in Table 2.

The optimal parameters of the third-degree nonlinear PEA_3 with weighting $\mathbf{w}=[1\ 1\ 1]$, for a person with mass $M=85$ kg (typical value for a patient in the VA Hospital), are

$$T_p^* = -\Theta_3^T \mathbf{k}_p^*, \quad \mathbf{k}_p^* = [41\ \ 301\ \ 617\ \ 439]^T \tag{17}$$

The design of the cam device to achieve this nonlinearity is discussed next.

4 Cam Device

The working principle of the cam-follower mechanism is illustrated in Fig. 10. This section describes the cam design problem, the selection of the device parameters, and the integration into a powered ankle prosthesis.

4.1 Cam Design Problem. The cam shape is affected by the cam-follower displacement s needed to generate a specified torque T_c, expressed as

$$T_c = -N_y b = -(N\cos\phi)b = -(k_c s)b \tag{18}$$

where N is the normal force acting on the cam, N_y is the vertical component of the normal force, ϕ is the pressure angle (e.g., the

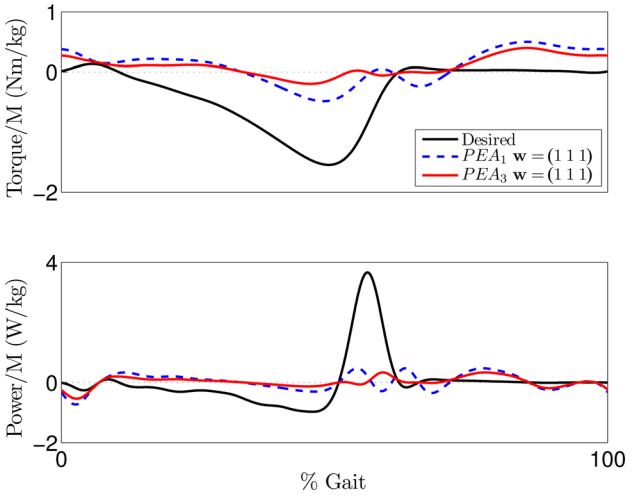

Fig. 9 Comparison of normalized actuator torque T_a/M and power P_a/M for optimal linear PEA_1 with those for the optimal, third-degree nonlinear PEA_3 with w = [1 1 1]

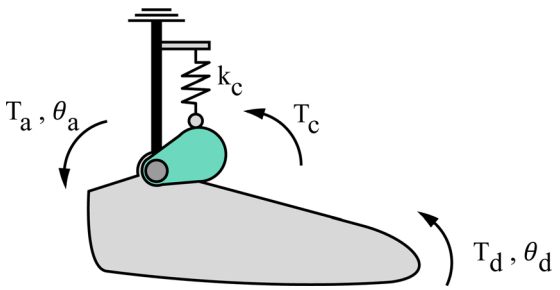

Fig. 10 Design concept for cam-based parallel component. The cam is fixed to the foot segment and displaces the spring attached to the shank segment.

angle between the normal force N and the line of action of the follower), k_c is the spring constant of the follower spring, s is the displacement of the follower (which also corresponds to the change in the follower-spring length), and b is the horizontal distance from the cam axis of rotation (point O in Fig. 11) to the instant center of velocity of the cam and the follower (point A in Fig. 11), which is a point that moves with the cam and has the same velocity, v_f, as the follower. Note that the distance b is numerically equal to the rate of change $s' = ds/d\theta_d$ of the follower displacement s [33], because

$$v_f = \frac{ds}{dt} = \left(\frac{d\theta_d}{dt}\right) b \tag{19}$$

which results in

$$s' = \frac{ds}{d\theta_d} = b \tag{20}$$

Hence, the cam torque T_c in Eq. (18) maybe rewritten as

$$T_c = -k_c s s' \tag{21}$$

The cam torque T_c should match the optimal nonlinear passive torque T_p^* (Eq. (17)), which leads to

$$-k_c s s' = -\sum_{i=0}^{n} \theta_d^i k_{p_i}^* \tag{22}$$

Downloaded From: http://medicaldevices.asmedigitalcollection.asme.org/ on 12/15/2014 Terms of Use: http://asme.org/terms

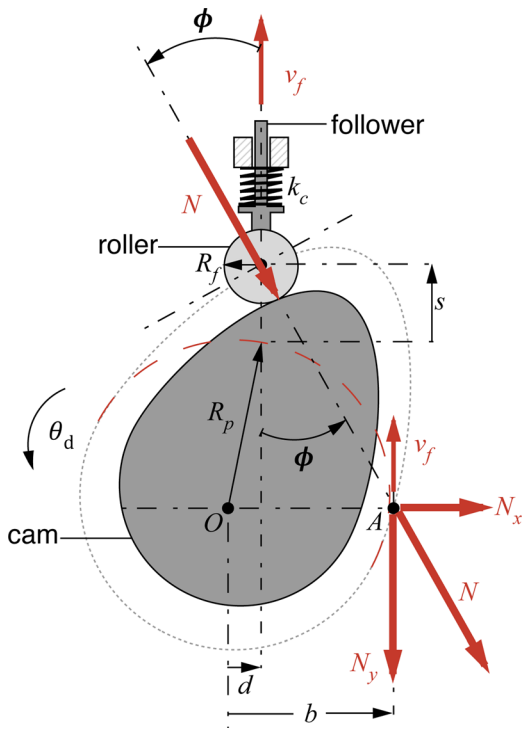

Fig. 11 Schematic of the cam-follower mechanism adapted from Ref. [33]. The cam rotates about point *O* (the center of the prime radius R_p), which is *d* away from the line of action of the cam follower, whose displacement is *s* and velocity is v_f. The pressure angle ϕ is the angle between the normal force *N* and the follower's line of action. The instant center of rotation is *A*, which is *b* away from the center of rotation *O*.

Integrating Eq. (22) yields an expression for the follower displacement s as a function of the desired angular displacement θ_d

$$-k_c s\frac{ds}{d\theta_d} = -\sum_{i=0}^{n}\theta_d^i k_{p_i}^*$$

$$\int s ds = \int \frac{1}{k_c}\sum_{i=0}^{n}\theta_d^i k_{p_i}^* d\theta_d$$

$$s = \left(\frac{2}{k_c}\sum_{i=0}^{n}\frac{1}{i+1}\theta_d^{i+1}k_{p_i}^* + c\right)^{1/2} \quad (23)$$

$$= [f(\theta_d) + c]^{1/2} \quad (24)$$

where c is a constant and the function f is independent of c.

Large side forces on the cam-roller can lead to jamming. To avoid this, the normal force (N in Fig. 11) on the roller should be aligned with the motion v_f of the follower, i.e., the pressure angle ϕ between them must remain sufficiently small (e.g., max $|\phi| < 30$ deg [33]). The pressure angle ϕ can be expressed as

$$\phi = \tan^{-1}\frac{b-d}{\sqrt{R_p^2 - d^2 + s}} = \tan^{-1}\frac{s'-d}{\sqrt{R_p^2 - d^2 + s}} \quad (25)$$

where the follower displacement, s, is given by Eq. (23), R_p is the prime radius of the cam, and d is the eccentricity of the cam, i.e., the distance from the cam rotation axis, denoted point O, to the line of action of the follower as shown in Fig. 11. Additionally, to ensure a single point of contact between the cam and the roller, the minimum radius of curvature ρ of the cam must be sufficiently greater than the radius of the roller R_f (e.g., min $|\rho| \geq 1.5R_f$ [33]). The radius of curvature ρ of the cam can be expressed as [33]

$$\rho = \frac{\left((R_p + s)^2 + s'^2\right)^{3/2}}{(R_p + s)^2 + 2s'^2 - s''(R_p + s)} \quad (26)$$

Thus, the two constraints in the cam design are

$$\min|\rho| \geq 1.5R_f, \quad \min|\phi| < 30\,\text{deg} \quad (27)$$

4.2 Selection of Cam Design Parameters. The parameters that can be chosen are the integration constant c in the cam profile s (see Eq. (23)), the prime radius R_p, the roller radius R_f, the eccentricity d, and the follower-spring constant k_c. To keep the cam size small, the prime radius and the roller radius R_f were chosen to be small—the selected prime radius was $R_p = 25$ mm and the roller radius was $R_f = 9.5$ mm (Smith Bearing Yoke Type Metric Cam Follower MYR-6-S).

The two constraints in Eq. (27) can be satisfied by choosing a sufficiently large integration constant c in Eq. (23). In particular, from Eq. (24), the follower displacement s increases with c while the derivatives of s with respect to the angular displacement θ_d decrease with increasing c because

$$s' = \frac{ds}{d\theta_d} = \frac{1}{2s}f'(\theta_d) \quad (28)$$

$$s'' = \frac{d^2 s}{d\theta_d^2} = -\frac{1}{4s^3}f'(\theta_d)^2 + \frac{1}{2s}f''(\theta_d) \quad (29)$$

and f', f'' are independent of c. This implies that as the integration constant c becomes large (alternatively, as s becomes large), the magnitude of the radius of curvature ρ tends to infinity since the numerator dominates in Eq. (26), i.e.,

$$\rho = \frac{\left((R_p + s)^2 + \frac{1}{4s^2}f'(\theta_d)^2\right)^{3/2}}{(R_p + s)^2 + \frac{3s + Rp}{4s^3}f'(\theta_d)^2 - \frac{s + R_p}{2s}f''(\theta_d)} \quad (30)$$

$$\approx (R_p + s) \quad \text{as} \quad s \to \infty$$

Similarly, as integration constant c becomes large, the pressure angle ϕ tends to zero since the denominator dominates in Eq. (25). Thus, both constraints can be satisfied by choosing a sufficiently large, integration constant c in Eq. (23).

The selected cam parameters (in Table 3) satisfy the constraints. For example, the effect of varying the eccentricity d and spring constant k_c on the pressure angle can be seen in Fig. 12, where isolines represent the maximum pressure angle ϕ (Eq. (25)), and the black dotted line denotes the maximum allowable pressure angle, max$|\phi| = 30$ deg. The selected cam parameters (denoted by the red dot in Fig. 12 for an off-the-shelf spring $k_c = 817$ kN/m, Anchor Lamina JIS Compression Spring

Table 3 Prototype cam design parameters

Prime radius R_p (mm)	25
Roller radius R_f (mm)	9.5
Follower stiffness k_c (kN/m)	817
Eccentricity d (mm)	8.75
Constant c (m^2)	1.25×10^{-5}
Max pressure angle (deg)	26
Min cam curvature (mm)	16

Downloaded From: http://medicaldevices.asmedigitalcollection.asme.org/ on 12/15/2014 Terms of Use: http://asme.org/terms

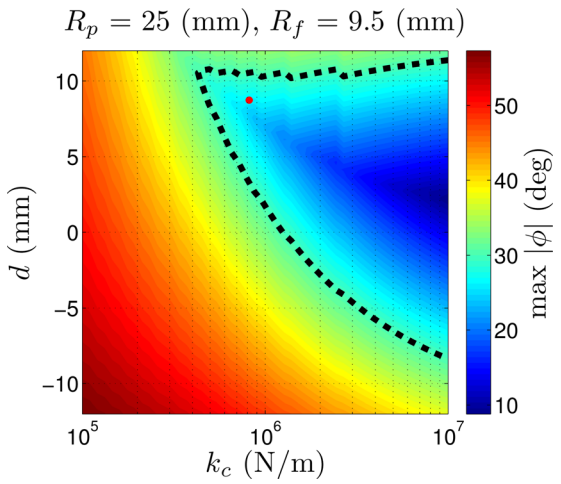

Fig. 12 Pressure angle ϕ for different follower stiffness k_c and eccentricity d. Dotted line denotes maximum allowable pressure angle, max$|\phi|$ = 30 deg. The red dot denotes the prototype configuration.

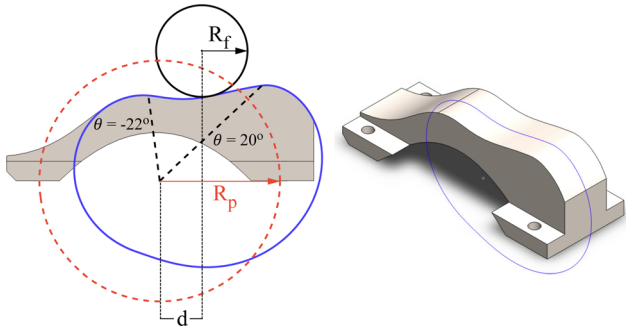

Fig. 13 Cam prototype for PEA$_3$ with parameters in Table 3. The black dashed lines represent the boundaries of the functional area: −22 deg for plantarflexion and 20 deg for dorsiflexion.

95–5060), satisfies the pressure angle constraint in Eq. (27). Also, the constraint on the radius of curvature ρ in Eq. (27) is satisfied by choosing the integration constant c to yield a sufficiently large minimum radius of curvature min$|\rho| = 16$ mm that is more than 1.5 times the roller radius $R_f = 9.5$ mm. The resulting cam shape is shown in Fig. 13.

4.3 Device Integration. The cam can be exchanged (if needed), since it is attached to the ankle link by four screws. Moreover, a specially designed ramp section is incorporated into the cam shape as shown in Fig. 13, which allows the spring to be unloaded by sufficiently rotating the ankle in the plantarflex direction. The main components of the device (including those in the follower assembly) are shown in Fig. 14(*a*), and an image of the actual device is provided in Fig. 14(*b*). The active component (e.g., drive train) is realized with an EC-22, 100 W, Maxon motor with a 5.4:1 planetary gearhead coupled to a ball screw (4 mm lead Thomas NEFF rolled ball screw). The drive train is protected from shocks by the foot, which acts as a leaf spring (Ossur LP Vari-Flex). Moreover, a standard pyramid adapter, used to attach the device to a patient's prosthetic socket, is included on the top of the device.

5 Experimental Results

To verify the elastic response achieved by the cam-follower mechanism, the powered ankle prosthesis (with the drive train and composite foot removed) was subjected to static loading experiments using an Instron 5585H electromechanical materials testing machine. The experimental setup to angularly deflect the ankle joint and measure the resulting torque is shown in Fig. 15.

5.1 Obtaining the Elastic Response. The experimental cam torque $\hat{T}_c$ can be calculated in terms of the reaction forces (F_x and F_z measured with a 6DOF load cell (AMTIMC3A), see Fig. 15(*a*)) by taking the moment about the ankle-joint center O and using Eq. (18) as

$$\hat{T}_c = -\bar{y}F_x - \bar{x}F_y \tag{31}$$

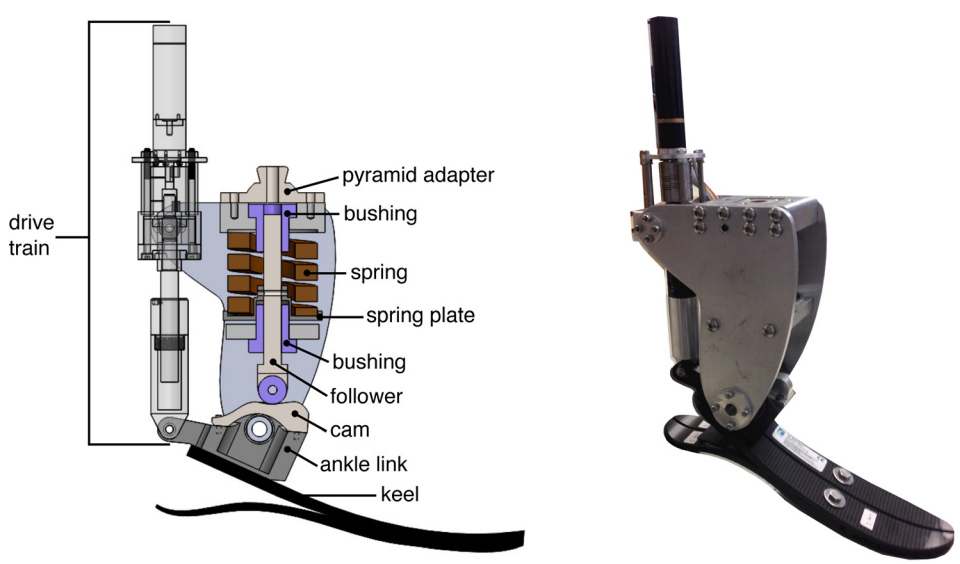

Fig. 14 Images of the prototype powered ankle prosthesis. (*a*) Cross section with major components labeled. (*b*) Picture of actual device.

Downloaded From: http://medicaldevices.asmedigitalcollection.asme.org/ on 12/15/2014 Terms of Use: http://asme.org/terms

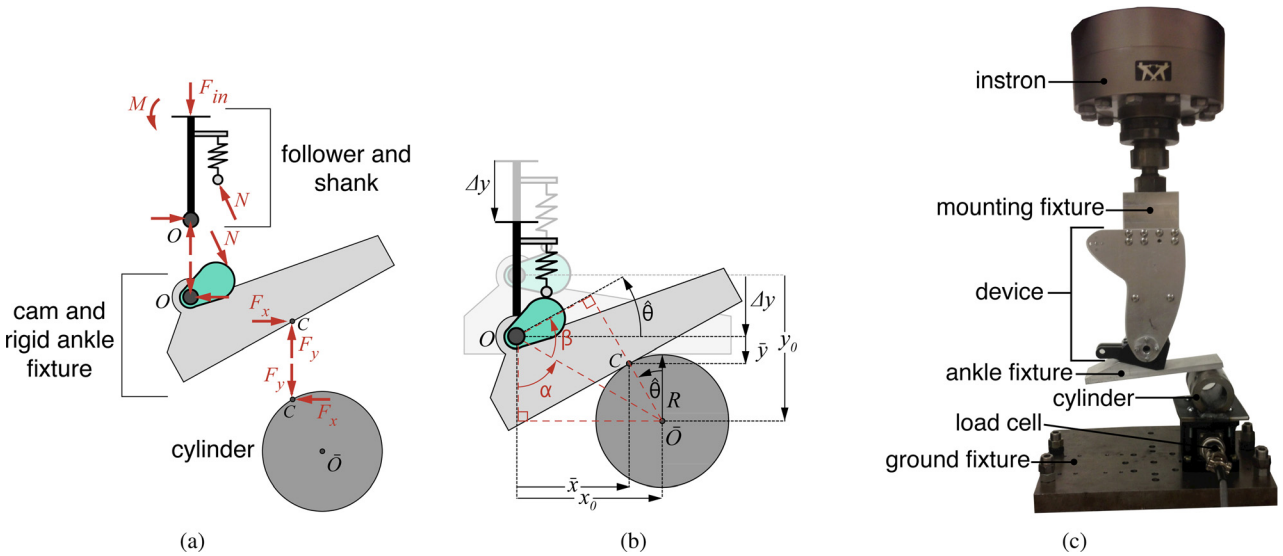

Fig. 15 Images detailing the static loading experiment. (*a*) Free body diagram of static loading experiment. (*b*) Schematic of static loading experiment illustrating the geometry and the angular displacement $\hat{\theta}$, caused by input displacement Δy. (*c*) Image of experimental setup.

where $\bar{y}$ and $\bar{x}$ are the vertical and horizontal distances from ankle-joint center O to the contact point C between the ankle fixture and the cylinder, as shown in Fig. 15(*b*). From the geometrical constraints, $\bar{y}$ and $\bar{x}$ are calculated as

$$\begin{aligned} \bar{x} &= x_0 - R\sin\hat{\theta} \\ \bar{y} &= y_0 - \Delta y - R\left(1 - \cos\hat{\theta}\right) \end{aligned} \tag{32}$$

where $\hat{\theta}$ is the experimentally measured rotational displacement of the ankle joint, and y_0 and x_0 are the initial vertical and horizontal distances from the ankle-joint center O to the cylinder center $\bar{O}$, respectively (see Fig. 15(*b*)), Δy is the measured vertical displacement imposed by the Instron machine, and R is the diameter of the cylinder in Fig. 15(*b*). The distances y_0 and x_0 are known from the geometry of the system. The rotational displacement $\hat{\theta}$ of the ankle joint, due to the vertical displacement Δy, can be calculated as

$$\hat{\theta} = \frac{\pi}{2} - [\pi - (\alpha + \beta)] = \alpha + \beta - \frac{\pi}{2} \tag{33}$$

where

$$\sin\alpha = \frac{x_0}{h}, \quad \sin\beta = \frac{y_0}{h}, \quad h = \sqrt{(y_0 - \Delta y)^2 + x_0^2} \tag{34}$$

5.2 Nominal Results. The experimentally obtained elastic response, e.g., the cam torque $\hat{T}_c$ from Eq. (31) versus angular displacement $\hat{\theta}$ from Eq. (33), for three loading and unloading cycles is compared with the desired elastic response (from Eq. (17)) in Fig. 16. Significant deviation ($\%E_{\max} = 33.8\%$) from the optimal profile is seen where the max error $\%E_{\max}$ is calculated as

$$\%E_{\max} = \frac{\max\limits_{i\in\{1,\ldots,p\}} \left|T_p^*[i] - \hat{T}_c[i]\right|}{\max\limits_{i\in\{1,\ldots,p\}} \left|T_p^*[i]\right|} \times 100\% \tag{35}$$

where $[i]$ represents the ith data sample, p is the total number of samples, $\hat{T}_c[i]$ are the experimentally determined torque values given by Eq. (31), and $T_p^*[i]$ correspond to the desired (optimal) torque at the measured angular displacement $\hat{\theta}[i]$.

5.3 Corrected Results. To correct the cam response, shims (spacers) were placed between the top of the spring and the support structure (see Fig. 14(*a*)) to adjust deviations in the follower-spring preload. The torque $\tilde{T}_c$ with a shim thickness of $\bar{s}$ can be found from Eq. (21) as

$$\tilde{T}_{c,\bar{s}} = -\tilde{k}_c(s + \bar{s})s' \tag{36}$$

where $\tilde{k}_c = 722\,\text{kN/m}$ is the measured spring constant found using a static load test, which is different from the manufacturer-reported nominal value of $k_c = 817\,\text{kN/m}$ used in the design. First, the potential error in the preload is estimated in terms of a shim thickness $\bar{s}_1$ by fitting the elastic response with a shim in Eq. (36) to the experimental elastic response through the following minimization:

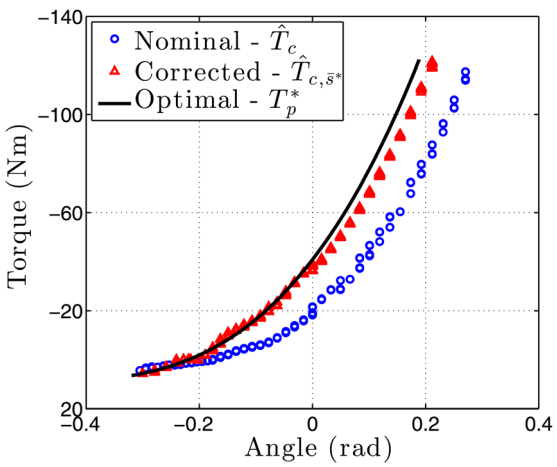

Fig. 16 Experimental validation of cam elastic response. The circles represent the experimental data points for the nominal case. The triangles are experimental data points with a 3 mm shim added to the device.

Downloaded From: http://medicaldevices.asmedigitalcollection.asme.org/ on 12/15/2014 Terms of Use: http://asme.org/terms

$$\min_{\bar{s}} \sum_{i=1}^{p} \left(\hat{T}_c[i] - \tilde{T}_{c,\bar{s}}[i]\right)^2 \tag{37}$$

where $[i]$ represents the ith data sample, and p is the total number of samples, $\widehat{T}_c$ are the experimentally determined torque values given by Eq. (31), and $\tilde{T}_{c,\bar{s}}[i]$ corresponds to the torque at the measured angular displacement $\widehat{\theta}[i]$. The optimal shim $\bar{s}_1$ that solves the minimization problem in Eq. (37), corresponds to the inherent error in the preload of the device. Next, the required preload is estimated in terms of a shim thickness $\bar{s}$ by fitting the elastic response with a shim in Eq. (36) to the optimal elastic response through the following minimization:

$$\min_{\bar{s}} \sum_{i=1}^{p} \left(T_p^*[i] - \tilde{T}_{c,\bar{s}}[i]\right)^2 \tag{38}$$

where $T_p^*[i]$ and $\tilde{T}_{c,\bar{s}}[i]$ correspond to the optimal torque and shim-based torque, respectively, calculated at different measured angular displacement values $\hat{\theta}[i]$. The optimal solution, $\bar{s}_2$ that solves the minimization problem in Eq. (38), corresponds to the preload needed to correct the elastic response due to error in the follower-spring's spring constant. Thus, the shim thickness $\bar{s}^*$ needed to correct for errors in the cam's elastic response can be calculated as

$$\bar{s}^* = \bar{s}_2 - \bar{s}_1 \approx 3 \text{ mm} \tag{39}$$

After adding the shims, the experiment to determine the elastic response was repeated and the results are shown in Fig. 16. The maximum percent error (Eq. (35)) of the ankle with the shims is 9.9%.

5.4 Future Efforts. Improvements to the modeling and optimization presented in this article are possible, for example, by including the motor dynamics and inertial effects into the optimization. Although this article focused exclusively on the parallel element (since it directly affects the torque), the approach could be extended to include optimization of combinations of nonlinear serial and PEAs. The current device will serve as a testbed for active testing. Toward this, our ongoing efforts include the development of control algorithms.

6 Conclusion

The results from this article show that the elastic response of a biological ankle, at self-selected walking gait, is well approximated using nonlinear elements. As a result, a nonlinear element can substantially decrease the requirements on the active component when compared with a linear element. In particular, an optimal nonlinear element can substantially reduce the positive energy (~40%), peak positive power (~29%), and peak torque (~21%) when compared to an optimal linear element. A cam-based passive element was designed to realize the nonlinear element, which matched the desired nonlinear response to within 10%.

Acknowledgment

This research was supported by the Department of Veterans Affairs, Rehabilitation Research and Development Service, Grant No. A9243C, and by the Department of Education Grant No. GAANN P200A130025, Image-based Biomechanics Modeling Program.

References

[1] U.S. Bureau of the Census, 1995, *Statistical Abstract of the United States*, 115th ed., U.S. Bureau of the Census, Washington, DC, p. 145.
[2] Fletcher, D. D., Andrews, K., Hallett, J., Butters, M., Rowland, C., and Jacobsen, S., 2002, "Trends in Rehabilitation After Amputation for Geriatric Patients With Vascular Disease: Implications for Future Health Resource Allocation," Arch. Phys. Med. Rehabil., **83**(10), pp. 1389–1393.
[3] Sun, J., and Voglewede, P. A., 2013, "Powered Transtibial Prosthetic Device Control System Design, Implementation, and Bench Testing," ASME J. Med. Devices, **8**(1), p. 011004.
[4] Versluys, R., Beyl, P., Van Damme, M., Desomer, A., Van Ham, R., and Lefeber, D., 2009, "Prosthetic Feet: State-of-the-Art Review and the Importance of Mimicking Human Ankle-Foot Biomechanics," Disability Rehabil. Assistive Technol., **4**(2), pp. 65–75.
[5] Morgenroth, D. C., Segal, A. D., Zelik, K. E., Czerniecki, J. M., Klute, G. K., Adamczyk, P. G., Orendurff, M. S., Hahn, M. E., Collins, S. H., and Kuo, A. D., 2011, "The Effect of Prosthetic Foot Push-Off on Mechanical Loading Associated With Knee Osteoarthritis in Lower Extremity Amputees," Gait Posture, **34**(4), pp. 502–507.
[6] Segal, A. D., Zelik, K. E., Klute, G. K., Morgenroth, D. C., Hahn, M. E., Orendurff, M. S., Adamczyk, P. G., Collins, S. H., Kuo, A. D., and Czerniecki, J. M., 2012, "The Effects of a Controlled Energy Storage and Return Prototype Prosthetic Foot on Transtibial Amputee Ambulation," Hum. Mov. Sci., **31**(4), pp. 918–931.
[7] Hansen, A. H., Childress, D. S., Miff, S. C., Gard, S. A., and Mesplay, K. P., 2004, "The Human Ankle During Walking: Implications for Design of Biomimetic Ankle Prostheses," J. Biomech., **37**(10), pp. 1467–1474.
[8] Sup, F., Bohara, A., and Goldfarb, M., 2008, "Design and Control of a Powered Transfemoral Prosthesis," Int. J. Rob. Res., **27**(2), pp. 263–273.
[9] Dermitzakis, K., Carbajal, J. P., and Marden, J. H., 2011, "Scaling Laws in Robotics," Procedia Comput. Sci., **7**, pp. 250–252.
[10] Vanderborght, B., Albu-Schaeffer, A., Bicchi, A., Burdet, E., Caldwell, D., Carloni, R., Catalano, M., Eiberger, O., Friedl, W., Ganesh, G., Garabini, M., Grebenstein, M., Grioli, G., Haddadin, S., Hoppner, H., Jafari, A., Laffranchi, M., Lefeber, D., Petit, F., Stramigioli, S., Tsagarakis, N., Damme, M. V., Ham, R. V., Visser, L., and Wolf, S., 2013, "Variable Impedance Actuators: A Review," Rob. Auton. Syst., **61**(12), pp. 1601–1614.
[11] Jutte, C. V., and Kota, S., 2008, "Design of Nonlinear Springs for Prescribed Load–Displacement Functions," ASME J. Mech. Des., **130**(8), p. 081403.
[12] Au, S., and Herr, H., 2008, "Powered Ankle-Foot Prosthesis," IEEE Rob. Autom. Mag., **15**(3), pp. 52–59.
[13] Haeufle, D., Taylor, M., Schmitt, S., and Geyer, H., 2012, "A Clutched Parallel Elastic Actuator Concept: Towards Energy Efficient Powered Legs in Prosthetics and Robotics," 4th IEEE RAS & EMBS International Conference on Biomedical Robotics and Biomechatronics (BioRob 2012), Rome, Italy, June 24–27, pp. 1614–1619.
[14] Rouse, E. J., Mooney, L. M., Martinez-Villalpando, E. C, and Herr, H. M., 2013, "Clutchable Series-Elastic Actuator: Design of a Robotic Knee Prosthesis for Minimum Energy Consumption," IEEE International Conference on Rehabilitation Robotics (ICORR 2013), Seattle, WA, June 24–26.
[15] Williams, R. J., Hansen, A. H., and Gard, S. A., 2009, "Prosthetic Ankle-Foot Mechanism Capable of Automatic Adaptation to the Walking Surface," ASME J. Biomech. Eng., **131**(3), p. 035002.
[16] Nickel, E. A., Hansen, A. H., and Gard, S. A., 2012, "Prosthetic Ankle-Foot System That Adapts to Sloped Surfaces," ASME J. Med. Devices, **6**(1), p. 011006.
[17] Thorson, I., and Caldwell, D., 2011, "A Nonlinear Series Elastic Actuator for Highly Dynamic Motions," 2011, IEEE/RSJ International Conference on Intelligent Robots and Systems (IROS), San Francisco, CA, Sept. 25–30, pp. 390–394.
[18] Wolf, S., and Hirzinger, G., 2008, "A New Variable Stiffness Design: Matching Requirements of the Next Robot Generation," IEEE International Conference on Robotics and Automation (ICRA 2008), Pasadena, CA, May 19–23, pp. 1741–1746.
[19] Vanderborght, B., Tsagarakis, N. G., Ham, R., Thorson, I., and Caldwell, D. G., 2011, "MACCEPA 2.0: Compliant Actuator Used for Energy Efficient Hopping Robot Chobino1D," Auton. Rob., **31**(1), pp. 55–65.
[20] Migliore, S. A., Brown, E. A., and DeWeerth, S. P., 2007, "Novel Nonlinear Elastic Actuators for Passively Controlling Robotic Joint Compliance," ASME J. Mech. Des., **129**(4), pp. 406–412.
[21] Copilusi, C., Dumitru, N., Rusu, L., and Marin, M., 2010, "Cam Mechanism Kinematic Analysis Used in a Human Ankle Prosthesis Structure," World Congress on Engineering, London, UK, June 30–July 2, pp. 1316–1320.
[22] Legro, M., Reiber, G., del Aguila, M., Ajax, M., Boone, D., Larsen, J., Smith, D., and Sangeorzan, B., 1999, "Issues of Importance Reported by Persons With Lower Limb Amputations and Prostheses," J. Rehabil. Res. Dev., **36**(3), pp. 155–163.
[23] Robert Brown, W., and Galip Ulsoy, A., 2013, "A Maneuver Based Design of a Passive-Assist Device for Augmenting Active Joints," ASME J. Mech. Rob., **5**(3), p. 031003.
[24] Palmer, M. L., 2002, "Sagittal Plane Characterization of Normal Human Ankle Function Across a Range of Walking Gait Speeds," Master's thesis, Department Mechanical Engineering, Massachusetts Institute of Technology, Cambridge, MA.
[25] Whittle, M. W., 2007, *Gait Analysis: An Introduction*, 4th ed., Butterworth Heinemann, Oxford, UK.
[26] Mettin, U., La Hera, P. X., Freidovich, L. B., and Shiriaev, A. S., 2009, "Parallel Elastic Actuators as a Control Tool for Preplanned Trajectories of Underactuated Mechanical Systems," Int. J. Rob. Res., **29**(9), pp. 1186–1198.

Downloaded From: http://medicaldevices.asmedigitalcollection.asme.org/ on 12/15/2014 Terms of Use: http://asme.org/terms

[27] Grimmer, M., Eslamy, M., Gliech, S., and Seyfarth, A., 2012, "A Comparison of Parallel and Series Elastic Elements in an Actuator for Mimicking Human Ankle Joint in Walking and Running," IEEE International Conference on Robotics and Automation (ICRA 2012), St. Paul, MN, May 14–18, pp. 2463–2470.
[28] Mathijssen, G., Cherelle, P., Lefeber, D., and Vanderborght, B., 2013, "Concept of a Series-Parallel Elastic Actuator for a Powered Transtibial Prosthesis," Actuators, **2**(3), pp. 59–73.
[29] Hollander, K. W., Ilg, R., Sugar, T. G., and Herring, D., 2006, "An Efficient Robotic Tendon for Gait Assistance," ASME J. Biomech. Eng., **128**(5), pp. 788–791.
[30] Hitt, J. K., Sugar, T. G., Holgate, M., and Bellman, R., 2010, "An Active Foot-Ankle Prosthesis With Biomechanical Energy Regeneration," ASME J. Med. Devices, **4**(1), p. 011003.
[31] Pratt, G., and Williamson, M., 1995, "Series Elastic Actuators," IEEE/RSJ International Conference on Intelligent Robots and Systems, Pittsburgh, PA, Aug. 5–9, pp. 399–406.
[32] Boyd, S., and Vandenberghe, L., 2004, *Convex Optimization*, Cambridge University Press, New York.
[33] Norton, R. L., 2009, *Cam Design and Manufacturing Handbook*, Industrial Press, New York.

Downloaded From: http://medicaldevices.asmedigitalcollection.asme.org/ on 12/15/2014 Terms of Use: http://asme.org/terms